Electronic Research Archive

ERA, 33(12): 7999–8018.
DOI: 10.3934/era.2025352
Received: 18 September 2025
Revised: 20 December 2025
Accepted: 23 December 2025
Published: 25 December 2025

http://www.aimspress.com/journal/era

Research article

Effect of long-range connections on surface inhibition in V1 area based on large-scale neural network modeling

Peihan Wang[1], Fang Han[1,2,*] and Hao Yang[3]

[1] College of Information Science and Technology, Donghua University, Shanghai 201620, China
[2] School of Mathematics and Statistics, Ningxia University, Ningxia 750021, China
[3] Shanghai BOCHU Electronic Technology Co., Ltd, China

* **Correspondence:** Email: yadiahan@163.com.

Abstract: The differentiation of neural activity in the primary visual cortex (V1) for the edges and surface regions of stimuli is a key feature in representing visual information. This differentiation is closely related to the phenomenon of surface inhibition, where neural activity in central surface regions is suppressed relative to edges of square stimuli. However, due to the challenges in manipulating biological experiments and the limitations of simplified models, the detailed synaptic-level analysis of the regulatory mechanisms underlying this differentiation has not been revealed. In this study, a visual information transmission pathway from visual stimuli to the lateral geniculate nucleus (LGN) of the thalamus, and further to the input and output layers of V1, is constructed by using real biological anatomical data to investigate the regulatory mechanisms underlying the aforementioned neural activity differentiation. The model successfully replicates the surface inhibition characteristics observed in biological experiments: the input layer exhibits relatively uniform responses to both surface and edge stimuli, while the output layer shows strong activity in edge regions and suppressed activity in central surface regions, creating a "hole" effect. Through control experiments—specifically, by eliminating long-range connections in L2/3—we find that long-range connections in layer 2/3 of V1 are the necessary conditions for generating the surface inhibition phenomenon within this layer. Furthermore, modulating either the proportion or the spatial distribution of long-range connections in L2/3 can exert regulatory effects on the surface inhibition phenomenon. This not only facilitates our understanding of the neural mechanisms underlying visual processing but also demonstrates the advantages of computational modeling in elucidating internal cortical mechanisms that are difficult to manipulate in biological experiments.

Keywords: computational model; primary visual cortex; long-range connections; hole effect

1. Introduction

Vision is one of the most fundamental sensory channels through which organisms perceive their external environment. The processing of visual information begins with the retina capturing light signals, which are then preliminarily integrated by the lateral geniculate nucleus (LGN) before being transmitted to the primary visual cortex (V1) for further refinement. At the first stage of visual information processing, the V1 region performs foundational functions such as edge detection, directional selectivity encoding, the separation of surfaces and contours, and information integration，making it a critical entry point for understanding the neural mechanisms of visual perception [1–4]. Among these, V1's differentiated responses to "surface brightness" (uniformly bright regions in stimuli, often located at the stimuli center) and "edge contrast" (regions with abrupt brightness changes in stimuli) are of significant importance for subsequent higher-order cognitive functions such as visual feature extraction [5].

Previous biological experiments, which employed square stimuli as the visual input, have shown that neural representations of edges and surfaces differ in V1, which is known as surface inhibition [5–7]: the input layer of V1 is sensitive to both edge and surface neural responses, exhibiting relatively uniform response patterns; however, in the output layer, activity in the edge region is significantly higher than in the surface central region, with the latter showing a marked reduction in response, forming an "activity hole". Zweig et al. [7] found that the early responses of V1 to colored and non-colored squares were both edge-enhanced, but the differences became significant in the later stages: the central responses of non-colored squares gradually increased, and the speed slowed as the size increased, with responses spreading from the edges toward the center; colored squares maintained edge enhancement throughout, with no central filling or spreading, indicating that V1 has different representation mechanisms for the two types of surfaces. Yang et al. [6] found through experiments in the V1 region of awake macaques that the input layer exhibited similar response intensities to surfaces and edges, while the output layer showed an "hole" phenomenon characterized by enhanced edge response and inhibited central surface response. Additionally, the brightness encoding strategy shifted from surface dominance in the input layer to edge dominance in the output layer, closely related to non-local cortical inhibition. Their simplified computational model further confirmed that feedforward excitation alone cannot reproduce this phenomenon, while introducing intra-layer non-local inhibition can simulate inter-layer response differences, validating the necessity of an intralaminar inhibition mechanism. Zurawel et al. [5] found through voltage-sensitive dye imaging experiments in the V1 region of macaque monkeys that in neural activity induced by black-and-white square stimuli, edge regions responded more strongly than the center, black stimuli elicited significantly stronger responses than white stimuli, and corner responses were higher than those in the middle of the edge. The computational model they constructed integrated local contrast, positive and negative brightness modulation, and center-periphery interactions in the cortex, successfully explaining the aforementioned response differences and spatial modulation characteristics. However, the above physiological studies and computational studies cannot precisely elucidate the regulatory patterns of specific parameters in V1 for surface inhibition phenomena.

In recent years, large-scale, detailed computational models, by virtue of their deep integration of

biological anatomical and physiological details, have become reliable tools for deciphering the neural mechanisms of the primary visual cortex. Baspinar et al. [8] constructed a V1 model based on sub-Riemannian geometry, which integrated the receptive field properties of orientation, frequency, and phase features, revealing the neural coding rules of multi-feature integration and breaking the limitations of single-feature models. Chen et al. [9] built a mouse V1 model based on massive neural data, adopting diverse neuron types and complex connection structures. This model exhibits the unique robustness and versatility of biological visual systems, clarifying the regulatory mechanisms by which V1's laminar structure and neuronal diversity contribute to noise resistance. Billeh et al. [10] constructed a finely simulated structure of the mouse primary visual cortex, containing approximately 230,000 neurons divided into 6 cortical layers and 17 neuron subtypes. This model can reproduce visually driven neural activities observed in biological experiments under stimulus patterns such as flashes, images, and black regions. Influenced by these advances, we conducted detailed modeling focusing on the specific mechanisms of different layers in V1 [11,12]. For L2/3 [11], we investigated the mechanisms by which the properties of long-range horizontal connections modulate the properties of gamma oscillations regulated by the size of visual stimuli. For L4 [12], we explored the mechanisms underlying cross-inhibition induced by gratings in V1 and gamma oscillations, and found that feedforward pathways induce cross-inhibition, while the push-pull organization of L4 affects gamma frequency. Through detailed modeling of the V1 region, these works have laid a foundation for deciphering the neural circuit mechanisms of different layers in V1.

Addressing the limitations that biological experiments struggle to finely resolve the regulatory rules of connection parameters, while simplified computational models overlook anatomical details, this study, based on the previous research paradigm of large-scale detailed modeling, constructed a biophysically constrained V1 circuit model. This model covers the visual pathway from visual stimuli through the lateral geniculate nucleus (LGN layer) to layers 4 and 2/3 of V1. Using this model, we reproduced the surface inhibition phenomenon in V1 and demonstrated the necessity of long-range connections in L2/3 for this phenomenon, further analyzing the regulatory rules of the proportion and spatial distribution of these long-range connections on surface inhibition. This provides a more detailed explanation of the surface inhibition phenomenon in V1 at the neural mechanism level and also offers a theoretical framework for understanding how the visual cortex optimizes information coding through connection characteristics. The structure of the remaining content of this paper is as follows. Section 2 elaborates on the model construction process (including visual stimuli, the LGN layer, V1 cortical neurons, and synapses) and simulation analysis methods. Section 3 presents the interlayer response differences in V1 and the regulatory effects of the proportion and spatial distribution of long-range connections on surface inhibition. Section 4 summarizes the research, discusses the advantages and limitations of the model, and proposes future research directions.

2. Model and methods

To investigate the hierarchical processing mechanisms of surface luminance in the primary visual cortex (V1), we construct a large-scale biophysical model that simulates the complete transmission pathway of visual information from the lateral geniculate nucleus (LGN) to the V1 cortex, which is shown in Figure 1a. The model is based on the hierarchical anatomical structure of the cat's primary visual cortex: visual stimuli are first encoded by neurons in the LGN layer and transmitted to the V1 input layer (L4 in this model) via excitatory feedforward projections. Visual information is further

transmitted from L4 to the output layer (L2/3), where the L2/3 layer integrates cross-columnar information through a unique network of long-range horizontal connections, with simultaneous excitatory feedback from L2/3 to L4. Both L4 and L2/3 contain 8000 excitatory neurons and 2000 inhibitory neurons, with their orientation preference shown in Figure 1b [13]. The synaptic connection patterns between neurons are jointly determined by the spatial distance of neurons, cell type, and receptive field properties.

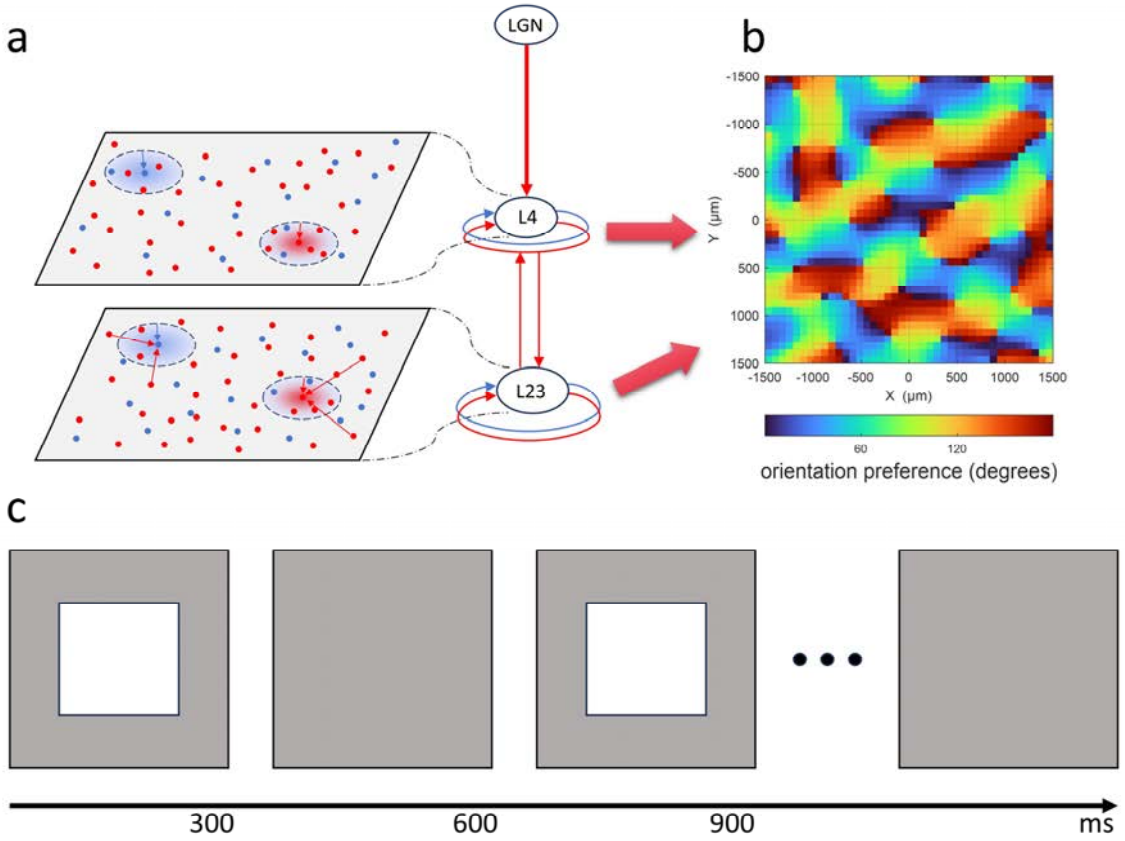


Figure 1. Model structure and stimulus paradigm. (a): Schematic diagram of the model's interlaminar pathways and intralaminar connection structure; red and blue denote excitatory and inhibitory neurons or connections, respectively. (b): Distribution of preferred orientations of V1 neurons. (c): Temporal sequence presentation paradigm of square visual stimuli.

2.1. Visual stimulation

In this study, visual stimuli is constructed with reference to the classic paradigms in mechanism research on surface brightness coding strategies [5,6], aiming to analyze the responses of neurons to stimulus surfaces and edges: a 4 × 4 white square is used, presented on a gray background (with brightness set to 50) for 300 ms, followed by a 300 ms blank period. The contrast of the square relative to the background brightness is set to 0.8, and the center of the square is aligned with the center of the receptive field. Subsequently, pixel points outside the square in the stimulus image are set to the background brightness, as shown in Figure 1c.

2.2. Lateral geniculate nucleus model

Based on the biophysical mechanisms of the primary visual cortex pathway, we construct a mathematical model of the lateral geniculate nucleus (LGN). LGN neurons are categorized into ON-center and OFF-center types: ON-center neurons respond strongly to bright regions surrounded by dark areas, while OFF-center neurons show the opposite response [14,15]. In the model, the receptive field values of these two neuron types are set to be opposite, i.e., $RF_{on} = -RF_{off}$. The model builds an LGN network containing 480 ON/OFF-center neurons, which are uniformly distributed over a 4 × 4 mm LGN plane. LGN neurons are modeled by the leaky integrate-and-fire (LIF) model:

$$C_m \frac{dV}{dt} = -g_L\left(V - E_L\right) + I_{in} \tag{1}$$

where the parameters are set as the membrane capacitance $C_m = 0.29$, leakage conductance $g_L = 0.029$, resting potential $E_L = -70mV$, and the refractory period is set to 2 ms.

The input current I_{in} in Eq (1) is calculated as the convolution of the LGN's receptive field and the input visual stimulus. The structure of the receptive field is defined as Eq (2), and the detailed parameters therein can be found in the study by Allen et al. [16]:

$$\begin{aligned}
&RF\left(x,t\right) = F_c\left(x\right)G_c\left(t\right) - F_s\left(x\right)G_s\left(t\right)\\
&F_c\left(x\right) = A_c e^{-x^2/2\sigma_c^2}\\
&F_s\left(x\right) = A_s e^{-x^2/2\sigma_s^2}\\
&G_c\left(t\right) = K_1 \frac{\left(c_1\left(t-t_1\right)\right)^{n_1} e^{-c_1\left(t-t_1\right)}}{{n_1}^{n_1} e^{-n_1}} - K_2 \frac{\left(c_2\left(t-t_2\right)\right)^{n_2} e^{-c_2\left(t-t_2\right)}}{{n_2}^{n_2} e^{-n_2}}\\
&G_s\left(t\right) = G_c\left(t-t_d\right)
\end{aligned} \tag{2}$$

2.3. Visual cortex model

Layer 4 in V1 receives feedforward inputs from the LGN, while layer 2/3 provides feedforward inputs to higher-order cortices. These two layers are most functionally important in V1 and we focus on the two layers in our model [17–19]. Existing biological experiments have shown that the number of neurons in each layer of V1 is roughly similar, and the ratio of excitatory to inhibitory neurons (E:I ratio) is approximately 4:1 [20,21]. To balance computational resources and biological details, we choose the ExpIF model to model the cortical neurons in L4 and L2/3 [12,22], with 8000 excitatory (E) neurons and 2000 inhibitory (I) neurons modeled in each layer. The ExpIF model is expressed as follows:

$$\tau_m \frac{\mathrm{d}V}{\mathrm{d}t} = -\left(V - E_L\right) + \Delta_T \exp\left(\frac{V - V_T}{\Delta_T}\right) - R_m g_E^n \left(V - E_{\mathrm{exc}}\right) - R_m g_I^n \left(V - E_{\mathrm{inh}}\right) \tag{3}$$

When the membrane potential exceeds the threshold, the neuron fires and resets to the resting potential of -70 mV. Specific parameter settings for the above model can be found in [13]. g_E^n and g_I^n

represent the synaptic conductances of excitatory and inhibitory synapses received by neuron *n*, respectively, and their specific details will be introduced in subsequent sections.

2.4. Synaptic model

The functional implementation of synapses depends on two key dimensions: the kinetic characteristics of synaptic conductance and the formation rules of synaptic connections, i.e., whether connections are established between neurons and the distribution of connection strengths [3,23]. Both aspects will be introduced in detail in the subsequent sections.

2.4.1. Synaptic conductance

Biological experiments have shown that excitatory synapses are mainly mediated by glutamate neurotransmitters via AMPA and NMDA receptors, whereas inhibitory synapses are mediated by GABA receptors [24]. Thus, in modeling, inhibitory synapses are defined as GABA synapses, and excitatory synapses are categorized into AMPA synapses and NMDA synapses based on receptor differences. The expressions for g_E^n and g_I^n in (3) are as follows:

$$\begin{aligned} g_I^n(t) &= \sum_{\sigma} g_{\sigma} \sum_{m\in \mathrm{Pre}} \sum_{j=1}^{k} G_{\mathrm{G}}\left(t-\left(t_{j,m}+t_{\mathrm{delay}}\right)\right) \\ g_E^n(t) &= \sum_{\sigma} g_{\sigma} \sum_{m\in \mathrm{Pre}} \sum_{j=1}^{k}\left(\rho_A^n G_{\mathrm{A}}\left(t-\left(t_{j,m}+t_{\mathrm{delay}}\right)\right)+\rho_N^n G_{\mathrm{N}}\left(t-\left(t_{j,m}+t_{\mathrm{delay}}\right)\right)\right) \\ &\quad + g_{\mathrm{LGN}} \sum_{m\in \mathrm{Pre}} \sum_{j=1}^{k} G_{\mathrm{A}}\left(t-\left(t_{j,m}+t_{\mathrm{delay}}\right)\right) \end{aligned} \tag{4}$$

Among these, σ denotes the type of presynaptic neurons, g_{σ} represents the base weight, *Pre* is the set of presynaptic neurons, *k* is the total number of spikes fired by neuron *m*, and t_{delay} is the delay time after neuron *m* fires. The excitatory conductance g_E^n comprises two components: inputs from LGN neurons and from excitatory neurons within the cortex. ρ_A^n and ρ_N^n are the proportions of AMPA and NMDA synapses, respectively, among the excitatory synapses. G_G, G_A and G_N describe the temporal dynamics of GABA, AMPA, and NMDA synaptic conductances, respectively, defined in the form of exponential differences [25]. Taking G_G as an example, its expression is as follows:

$$G_G = \frac{\exp\left(-t/\tau_{\mathrm{d},G}\right)-\exp\left(-t/\tau_{\mathrm{r},G}\right)}{\tau_{\mathrm{d},G}-\tau_{\mathrm{r},G}} \tag{5}$$

The definitions of G_A and G_N are analogous to this. τ_r and τ_{d} denote the rise and decay time constants, respectively. The specific settings of the aforementioned parameters are detailed in [13].

For the base weight g_{σ}, referring to previous modeling efforts [11,12,26] and the spiking activity of the model, the settings are as follows: $g_{EE}=0.05, g_{EI}=0.09, g_{IE}=0.20$ and $g_{II}=0.18$; and the feedforward weight from the LGN to L4 is 0.11.

2.4.2. Synaptic connection probability

The synaptic connection probability determines the likelihood of connection formation among neurons and is tightly constrained by multiple factors, including the neuron type, spatial location, functional properties, and so on [27–29]. In our model, the synaptic connection probabilities for thalamocortical and intracortical connections exhibit distinct patterns.

For the feedforward connections from the LGN to V1, the spatial distribution and connection strength of feedforward inputs are described by Gabor receptive fields [30], and are formulated as follows:

$$\begin{aligned} p(x,y,\theta) &= \exp\left(-\frac{x'^2+y'^2\gamma^2}{2\sigma^2}\right)\cos\left(2\pi x'\lambda+\psi\right) \\ x' &= x\cos\theta + y\sin\theta \\ y' &= -x\sin\theta + y\cos\theta \end{aligned} \tag{6}$$

Neurons in V1 form dense local networks based on the physical distance between them. Referring to the fitting of biological data by Antolik et al. [13], the local connection probability is defined as: $p_{\text{local}}(d)=\exp\left(-\alpha\sqrt{\theta^2+d^2}\right)$. The connection probabilities between different cortical neurons can be precisely set based on anatomical and physiological data.

In layer 4 (L4) of the visual cortex, neuronal connections are shaped by both physical distance and the push-pull effect. Specifically, E neurons prefer functionally similar neurons, while I neurons prefer opposite ones, with this selectivity rooted in Gabor receptive field correlation [31,32]. The push-pull probability follows a Gaussian distribution of this correlation c [12]: $p_{\text{push-pull}}(c)=\frac{1}{\sigma\sqrt{2\pi}}\exp\left(\frac{-(c-\mu)^2}{2\sigma^2}\right)$, with smaller σ indicating a stronger effect. L4 intra-layer connection probability is the product of local connection probability and push-pull probability.

In L2/3, pyramidal neurons form long-range connections with functionally similar neurons via extensive axonal networks [33,34]. Excitatory synapses here are divided into local and long-range types (boundary = 500 μm) based on relevant biological data [33,35], with the long-range ratio (proportion of long-range excitatory synapses) set to 40% by default. We use three Gaussian distributions to characterize their spatial distribution (inter-neuronal distance denoted as x) and orientation preference difference (denoted as Δo): $p(x,\Delta o)=p_{\text{local}}(x)+\alpha p_{\text{long}}(x)\cdot p_{\text{ori}}(\Delta o)$. The local component $p_{\text{local}}\sim N(0,0.27)$, the orientation preference component $p_{\text{ori}}\sim N(0,\pi/10)$, and for E-E and E-I synapses, the long-range components p_{long} follow $N(0,0.36)$ and $N(0,0.64)$, respectively. This enables wide-range visual information integration and functional consistency. The specific details of the aforementioned connection probabilities can be found in [11,13].

Combining model-size constraints and physiological constraints [36], and with reference to previous modeling work [11,12], the excitatory neurons are set to receive 800 synaptic inputs, and the inhibitory neurons receive 20% synapses. In terms of the proportion of synaptic types, excitatory synapses account for 80% of the total number of synapses, and inhibitory synapses account for 20%.

Moreover, inhibitory synapses only exist in intra-layer connections, while all inter-layer connections are excitatory and account for a quarter of the total excitatory synapses. The feedforward excitatory inputs from the LGN to L4 account for 10% of its total excitatory inputs, so as to maintain the cortical excitatory drive.

2.5. Analytical methods

Spike firing of neurons is a crucial factor in information encoding. When analyzing the spatial firing patterns in the primary visual cortex (V1), we refer to the analytical method by Yang et al. [6] and, combining it with the structure of our model, define the surface-edge response ratio (S/E ratio) to quantify the difference in population firing rates between the central and peripheral regions of V1. The calculation process of this index is as follows: the number of spikes fired by neuron *i* within the simulation time is denoted as $n_i(x,y)$, where (x,y) represents the position of the cortical neuron relative to the center of the visual stimulus. The surface region (S) is defined as the central region of the cortex: $d \le \delta_S, \delta_S = 500\mu m$; the edge region (E) is defined as the peripheral annular region of the cortex: $\delta_1 \le d \le \delta_2, \delta_1 = 1300\mu m, \delta_2 = 1500\mu m$, where $d = \max(|x|,|y|)$. The average firing rates (spikes/s) of the surface and edge regions are then given by: $R_S = \frac{\sum_{i\in S} n_i / C_S}{T}$, $R_E = \frac{\sum_{i\in E} n_i / C_E}{T}$, where C_S and C_E are the number of neurons in the surface and edge regions, respectively. Subsequently, the S/E ratio is defined as $S/E = R_S / R_E$.

To quantify the spatial distribution characteristics of long-range connections in layer 2/3 of the primary visual cortex, following the work by Yang et al. [11], we define the "connection completion ratio", with its expression given by: $r(l,c) = \frac{N_{formed}(l,c)}{N_c}$. Here, $N_{formed}(l,c)$ denotes the number of established long-range connections of type *c* within a range at a distance *l* from the center of L2/3, while N_c represents the total number of long-range connections of that type *c*. This metric characterizes the spatial accumulation pattern of a specific long-range connection type: if $r(l,c)$ rapidly approaches 1 as *l* increases, it signifies that this connection type is highly concentrated in the near-neighbor region; if the growth of $r(l,c)$ is slow, it reflects the extensive projection of such long-range connections.

3. Simulation results

3.1. Interlaminar differences in neural responses to edges and surfaces between the input and output layers of V1

Biological experiments have revealed differences in the neural responses of neurons across different layers of V1 to a given square stimulus. Neurons in the input layer of V1 show comparable levels of neural activation for surfaces and edges, whereas in the output layer, visually evoked activity

is significantly enhanced in edge regions, and a "hole" emerges in the response map of the square's central region—indicating that the response in the surface region of the output layer is suppressed [5,6].

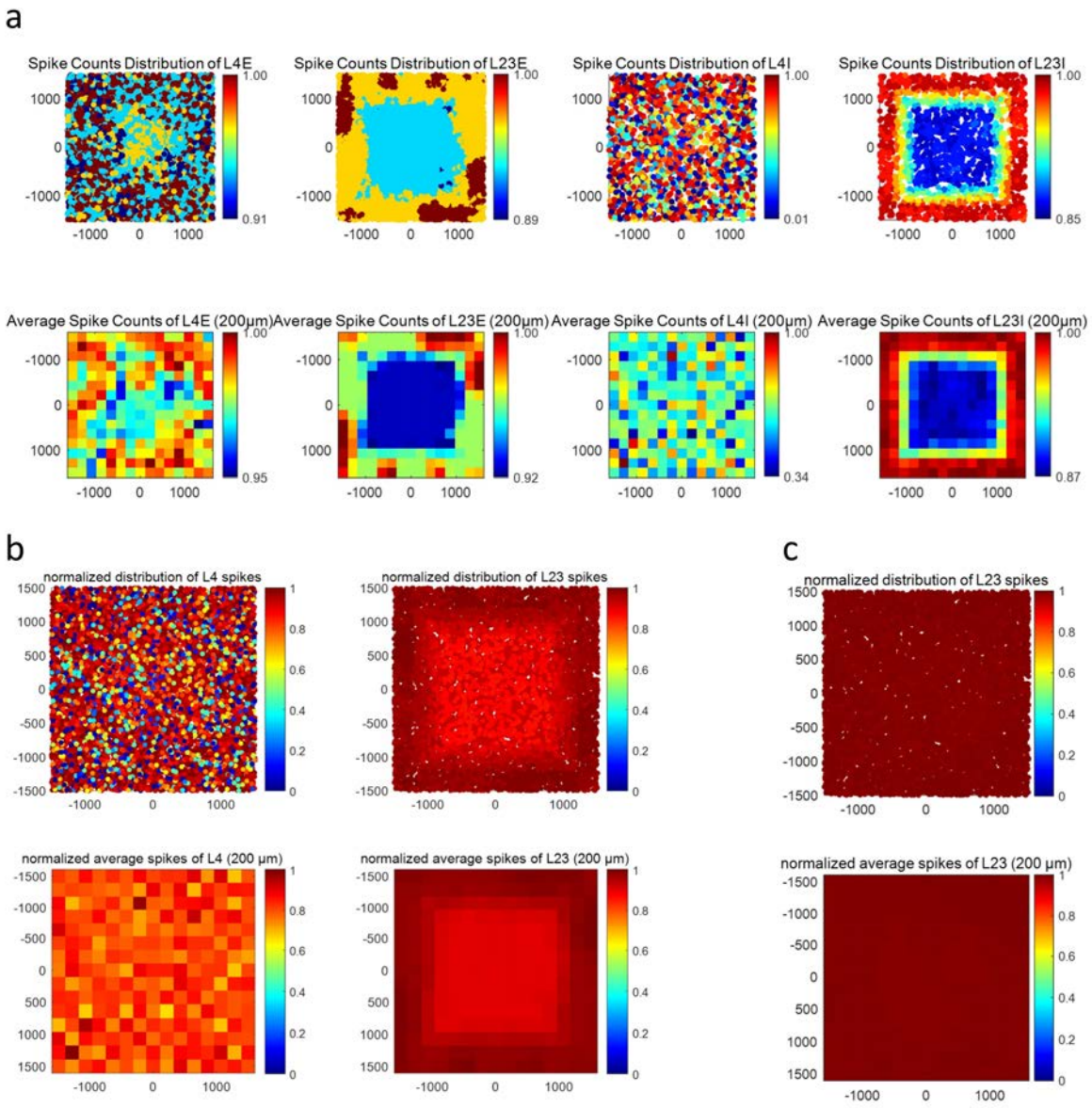


Figure 2. Cortical spiking under 40% long-Range ratio. (a): From left to right: Under 40% Long-Range Ratio, the spiking intensity distributions of L4E, L23E, L4I, and L23I neurons at different cortical positions (quantified as the spike counts over the entire simulation time), and the average spiking intensity distributions per 200 μm² (the same applies to the following figures). (b): Spiking distributions of L4 and L2/3 under 40% Long-Range Ratio. (c): Spiking distribution of L2/3 under 0% Long-Range Ratio.

Using the model constructed in Chapter 2, we successfully simulate these phenomena under the current connection conditions and parameter settings. In our model, the input layer of V1 corresponds to L4, and the output layer corresponds to L2/3. In the model, the long-range connection ratio in excitatory connections of L2/3 is set as 40% by default. Under this condition, L4 and L2/3 exhibit

distinct neuronal activity characteristics, with the simulation results shown in Figure 2. Figure 2a presents the spike count distributions of different neuron types in L4 and L2/3 (specifically, L4E and L2/3E represent excitatory neurons; L4I and L2/3I represents inhibitory neurons) and the average spike distributions are within 200μm grids. Among these, the spike count distribution maps of L4 neurons show that both L4E and L4I exhibit relatively uniform spatial distributions of spiking activity, with no obvious concentration or bias toward any regions; the corresponding average spike distribution maps also reflect this relative uniformity, with small differences in average spiking levels across regions. In contrast, in the spike count distribution maps of L2/3E and L2/3I, it is evident that neurons respond more strongly to edge regions, with significantly higher spike counts in edge regions than in the central surface region; the average spike distribution maps also show that the spiking levels in edge regions are significantly higher than those in the central region, indicating a high sensitivity to edge information. Furthermore, Figure 2b shows the results of overlaying L4E with L4I and L2/3E with L2/3I from Figure 2a, which also demonstrate the distinct spiking distribution characteristics between L4 and L2/3.

To further quantify this discrepancy, we calculate the surface-to-edge response ratio (S/E ratio) and found that the S/E ratio of L4 is higher than that of L2/3 (L4: 0.99; L2/3: 0.87). These results indicate that L4 exhibits relatively balanced processing of surface and edge information, whereas L2/3 demonstrates a stronger responsiveness to edge information coupled with a relatively weaker response to surface information.

For comparison, we eliminate long-range connections in L2/3 of the model (i.e., setting the long-range ratio to 0), while retaining intra-layer local connections and feedforward inputs from L4. In this condition, it is found that the aforementioned surface inhibition phenomenon disappears (Figure 2c): the spike distribution in L2/3 tends to be uniform, and the S/E ratio rebounds to a value close to that of L4. Our model breaks through the limitation of previous simplified models that only introduced non-local connections in the output layer [6], indicating that the non-local connections, namely long-range connections, in the output layer L2/3 are the necessary conditions for the occurrence of the surface inhibition phenomenon. The specific modulation rules will be discussed in detail in Sections 3.2 and 3.3.

3.2. Modulation of surface inhibition by the long-range connection ratio in L2/3

The previous section demonstrates the necessity of L2/3 long-range connections for surface inhibition through comparative experiments. In this section, we analyze the dynamic regulatory mechanism of long-range connections on surface inhibition by altering the ratio of L2/3 long-range connections.

Based on the simplified model framework established in previous studies [5,6], in the absence of feedback loops from L2/3 to L4 in the model, the spiking of L4 consistently exhibits a uniform pattern (Figure 3a), with the S/E ratio remaining stable (Figure 3b), indicating that its surface-edge responses are not affected by the long-range ratio of L2/3 in this condition. In contrast, the spiking distribution of L2/3 shows a trend where spiking activity in the central region continuously weakens as the long-range ratio increases (Figure 3a). Concurrently, the S/E ratio decreases (Figure 3b), revealing a pattern where a higher long-range ratio corresponds to a stronger surface inhibition effect.

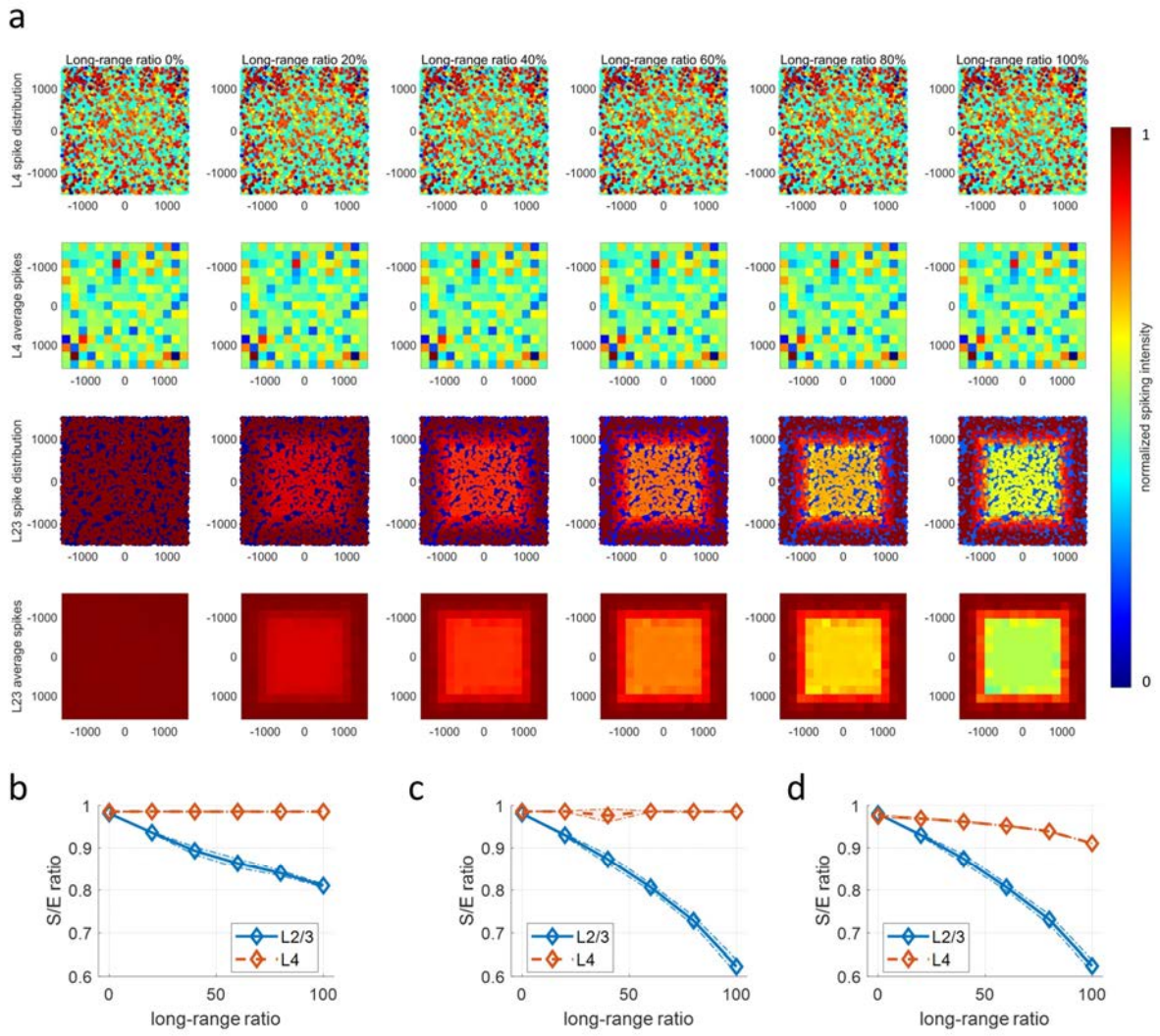


Figure 3. Modulation of cortical spiking by long-range ratio. (a): From top to bottom: Spiking intensity distributions and average spiking intensities of L4 neurons, and spiking intensity distributions and average spiking intensities of L2/3 neurons, under different Long-Range Ratios. (b): S/E Ratios of L2/3 and L4 under different Long-Range Ratios when there is no feedback from L2/3 to L4 in the model (where the solid lines represent the mean values of five independent experiments, and the area enclosed by dashed lines represents the standard deviation of the experiments; the same applies to the following figures). (c): S/E Ratio curves with reduced feedforward weights from L4 to L2/3, based on the condition in (b). (d): S/E Ratio curves with the introduction of feedback from L2/3 to L4, based on the condition in (c).

Furthermore, for the same long-range ratio, when the feedforward synaptic weights from L4 to L2/3 are reduced, the feedforward input decreases, causing L2/3 to passively increase its dependence on its intra-layer long-range connections. This leads to a more significant decrease in the S/E ratio of L2/3 as the long-range ratio increases, compared with the situation before the reduction (Figure 3c). This phenomenon reveals a competitive relationship between the feedforward input received by L2/3 and its intra-layer long-range connections: the lower the proportion of feedforward input, the more prominent the contribution of intra-layer long-range connections to surface inhibition, ultimately

resulting in a stronger surface inhibition effect in the central region.

Notably, with the introduction of excitatory feedback loops from L2/3 to L4, an interlaminar response pattern that more closely matches biological experimental characteristics is obtained: L2/3, which has already developed the surface inhibition effect, conveys regulatory signals to L4 through the feedback pathway, inducing a certain degree of surface inhibition in L4 as well. However, due to the attenuation of feedback signal intensity during transmission in the layers, the suppression effect in L4 is significantly weaker than that in L2/3. Ultimately, it is observed that the S/E ratio of L4 decreases slightly as the long-range ratio increases, exhibiting weak suppression; in contrast, the S/E ratio of L2/3 declines to a far greater extent than that of L4, showing strong suppression (Figure 3d). This feature is consistent with the observation in [6] that "surface inhibition exists in both the input and output layers of V1, but is more pronounced in the output layer," demonstrating that the model is capable of generating surface inhibition phenomena consistent with biological observation.

3.3. Modulation of surface inhibition by the spatial distribution of long-range connections in L2/3

With the default parameter settings of the model, the long-range connections in L2/3 exhibit a spatial distribution characteristic (Figure 4): short-range connections are dominated by excitatory-excitatory (E-E) synapses, while long-range connections are dominated by excitatory-inhibitory (E-I) synapses. Specifically, the synaptic weights of E-E connections ($\sigma_{EE}^2 = 0.36$) decay more rapidly with distance, whereas those of E-I connections ($\sigma_{EI}^2 = 0.64$) decay more slowly.

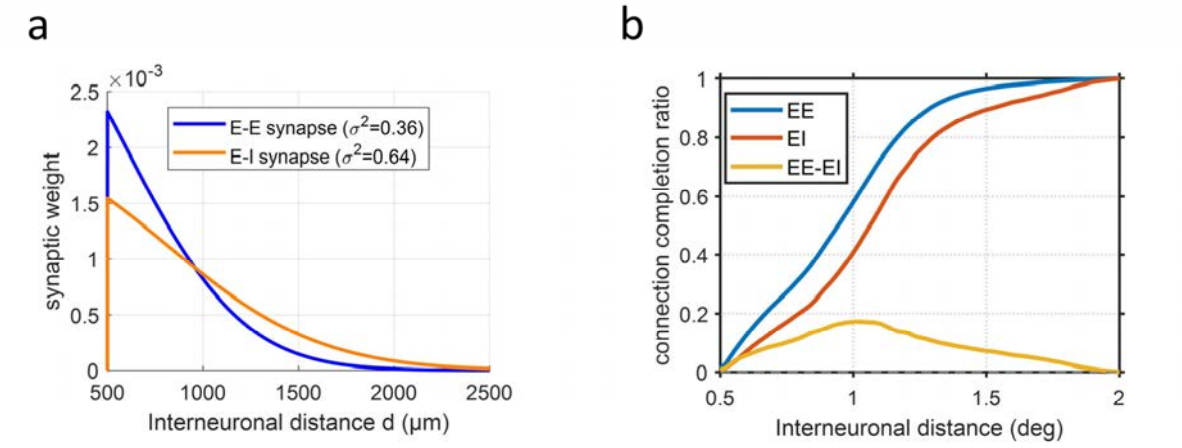


Figure 4. Model default long-range connection parameters. (a): Distribution of synaptic weights of E-E and E-I type long-range connections with respect to interneuron distance (assuming the same preferred orientation component for both types). (b): Completion ratios of E-E and E-I type long-range connections, and the difference between the two.

Anatomical and physiological studies have shown that intrinsic horizontal connections in V1, which link orientation-selective pyramidal cells with non-overlapping receptive fields, preferentially integrate collinear line segments—particularly when closely spaced—and amplify contour signals by

facilitating co-activation of these neurons, especially in the presence of complex backgrounds. [34,37]. With the current parameter settings, contour signals of stimuli at the edges are locally enhanced via short-range E-E connections, while inhibitory modulation is projected to the central region through long-range E-I connections, leading to the suppression of spiking in neurons within the central region. This ultimately results in the inhibition of spiking activity in the central surface region, exhibiting a "hollow" response pattern. Based on the introduction of feedback loops in Section 3.2, this section investigates the modulation of surface inhibition by the spatial distributions of these two types of long-range connections.

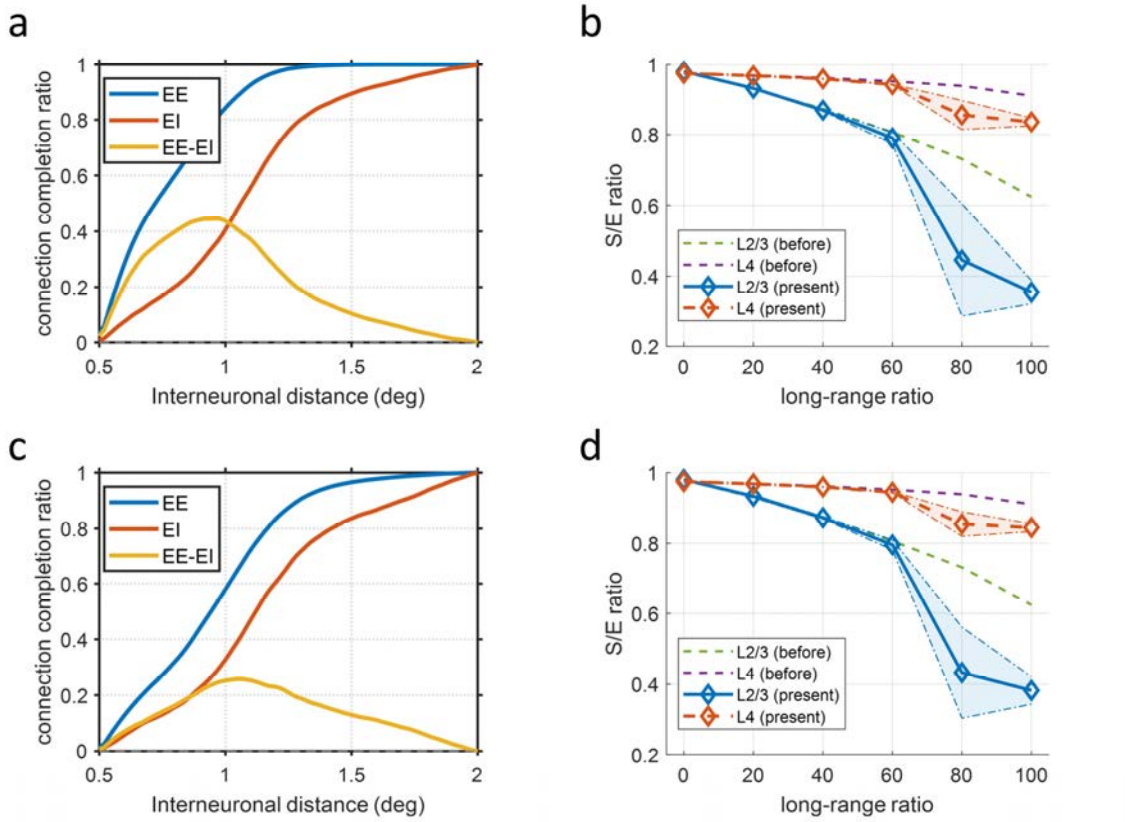


Figure 5. Modulation of Cortical Spiking by Long-Range Spatial Distribution. (a): Connection completion ratios when $\sigma_{EE}^2 = 0.16$ and $\sigma_{EI}^2 = 0.64$. (b): S/E curves under the condition in A (green and purple dashed lines represent the mean values of curves under default parameters; the same applies to the following figures). (c, d): Connection completion ratios and S/E curves when $\sigma_{EE}^2 = 0.36$ and $\sigma_{EI}^2 = 1$.

When the spatial coverage of E-E connections is reduced (with σ_{EE}^2 decreased to 0.16, Figure 5a), it causes E-E connections near the stimulus edges to rapidly concentrate within short distances. The excitatory drive from long-range E-E connections received by the central region is significantly weakened, and the region can only rely on local short-range connections to maintain its basal activity, with the excitatory input being attenuated. Therefore, the inhibitory effect of long-range E-I connections becomes relatively stronger, leading to further suppression of the spiking activity in the central region. This is manifested as a more pronounced decline in the S/E ratio curve compared to the previous situation (Figure 5b).

When the spatial coverage of E-I connections is extended (σ_{EI}^2 increased to 1, Figure 5c), the contour signals at the edges can disseminate inhibitory modulation to a more distant range via long-range E-I connections. This leads to a stronger inhibitory effect on the central region far from the edges compared to that under the default model parameters, resulting in a reduction in the intensity of its spiking activity. In Figure 4, as the proportion of long-range connections increases, the descending slope of the S/E ratio for the red curve is significantly steeper than that of the curve before the inhibitory modification (Figure 5d), verifying the enhanced suppression of the central surface induced by the expanded inhibitory range.

Both aforementioned modifications modulate surface inhibition by reshaping the excitatory-inhibitory synergy within the central region. Specifically, the contraction of the spatial range of E-E connections reduces the excitatory input to the central region, tilting the local E-I balance toward inhibition. This mechanism is consistent with findings showing that long-range excitatory connections can recruit local inhibition to generate surround suppression [38]. Conversely, the long-range extension of E-I connections enhances the inhibitory effect in the central region and facilitates the infiltration of inhibitory modulation. Critically, the spatial distribution of connections is a key determinant of network function, as studies have shown that the spatial profile of inhibitory connections—including their extent and the specific patterns of recruitment—directly influences cortical activity by modulating the local E-I balance [39]. In our model, both manipulations, though achieved through distinct changes in network topology (reducing excitatory drive versus enhancing inhibitory coverage), converge on a common mechanism: disrupting the finely tuned E-I balance in the central region. This underscores that surface inhibition is not merely a static phenomenon but is dynamically regulated by the spatial architecture of the network, which dictates how excitation and inhibition interact across the cortical surface.

4. Conclusions and discussion

In this study, a biologically detailed neural network model of the primary visual cortex (V1) is constructed to investigate the mechanisms by which surface inhibition in V1 is regulated by specific connectivity. Our model successfully recapitulates the surface inhibition phenomenon in V1: in the input layer (L4) of V1, neural activity levels across surface and edge regions are comparable, exhibiting relatively uniform responses; in contrast, the output layer (L2/3) shows enhanced neuronal activity in stimulus edge regions, whereas activity in the central region is attenuated, giving rise to a "hollow" response pattern. This is consistent with conclusions drawn from previous biological experiments [5–7]. Further experiments reveal that upon ablation of intra-layer long-range connections in L2/3, the surface inhibition phenomenon vanishes, indicating that long-range connections within L2/3 constitute a necessary condition for the emergence of surface inhibition.

Furthermore, by adjusting the proportion and spatial distribution of intra-layer long-range connections in L2/3, their regulatory mechanisms on the surface inhibition phenomenon are investigated. First, either directly increasing the proportion of long-range connections in L2/3 excitatory connections or reducing the feedforward input weights from L4 to L2/3 while keeping the long-range ratio constant leads to an increase in the proportion of long-range connections in L2/3, thereby enhancing the surface inhibition phenomenon. Regarding the spatial distribution of long-range connections, under the current default parameters, the spatial characteristics are manifested as short-range dominance of E-E connections and long-range dominance of E-I connections. Shortening the spatial coverage of E-E connections causes E-E connections to aggregate rapidly within short distances;

the central region, due to insufficient long-range excitatory input, exhibits weakened spiking activity. In contrast, extending the spatial coverage of E-I connections enables edge inhibitory signals to infiltrate regions closer to the center, enhancing the inhibitory effect thereon and similarly weakening the spiking activity in the central region. These two modifications to the spatial distribution of long-range connections both enhance the surface inhibition effect by disrupting the "excitatory-inhibitory balance" in the central region.

Yang et al. [6] proposed a simplified model based on biological experimental data, which only introduced simplified non-local inhibition in the output layer, focusing on verifying the existence of the non-local inhibition mechanism without analyzing the synergistic interaction between local and long-range connections. Zurawel et al. [5] recorded population responses in the V1 region of monkeys using voltage-sensitive dye imaging techniques and constructed a feedforward model from visual stimuli to V1 to explain the response patterns of V1 to black-and-white stimuli; however, their model did not subdivide the types of intra-layer connections. In contrast, the present study constructs a large-scale V1 model with more biological details. From a modeling perspective, it more elaborately dissects how surface inhibition is regulated through the properties of long-range connections, providing a more specific mechanistic explanation for biological experimental phenomena. This enables the analysis of intracortical mechanisms that are technically challenging to achieve in biological experiments. Nevertheless, the current phenomena depend on the structure and parameters of the model itself, and whether the same logic holds in the real biological primary visual cortex remains to be explored.

Notably, neural surface representation is an inter-areal process involving interactions between V1 and higher visual areas (e.g., V4, IT) rather than a purely intra-cortical mechanism [40]. The current model deliberately focuses on V1's internal long-range connections by simplifying inter-areal projections, and our findings may serve as a local mechanistic basis for the broader inter-cortical network underlying surface representation. Importantly, V1's L2/3 long-range connections may exhibit organizational parallels with the large-scale grouping mechanisms mediated by feedback projections from higher visual areas [41]. Layton et al. (2012) highlighted that higher areas (e.g., V4) integrate global figure information via expansive grouping fields, which might interact with primary visual areas (e.g., V1, V2) local connectivity dynamics to collectively shape surface representation. How such cross-level functional alignment contributes to visual processing remains an intriguing direction for further inquiry.

Additionally, it is worth noting that neural representation of surfaces is not limited to those with contrast-based edges—surfaces lacking such edges (e.g., kinetically defined surfaces formed by motion alone) can also evoke stable neural responses [42]. Layton et al. (2015) demonstrated that the visual system can rely on motion cues (e.g., texture accretion/deletion, shearing motion) to form kinetic edges and complete figure-ground segregation, even when luminance contrast between the surface and background is absent. The current study focuses on surfaces with contrast-based edges, and whether the regulatory mechanism of L2/3 long-range connections on surface inhibition can be extended to non-contrast edge-based surfaces remains to be explored. Future research may further expand the stimulus paradigm to include non-contrast edge scenarios, which will help verify the generalizability of the present findings and enrich our understanding of the universal neural mechanisms underlying surface representation.

Although the present model incorporates more abundant biological details compared to simplified models, it may still diverge from real biological systems. For instance, the simplification of neuronal types into broad excitatory and inhibitory categories may overlook the functional diversity of specific

subpopulations, as highlighted by the identification of specialized athorny pyramidal cells in hippocampal CA3 that fine-tune oscillatory dynamics [43]. Future models could introduce finer cell classifications to explore their unique contributions to visual processing. Furthermore, studies have demonstrated that synaptic plasticity between neurons dynamically adjusts with changes in time and stimulus patterns, a process critical for neural information processing and the development of visual functions [44,45]. Real neural activity may also be extensively influenced by neuromodulators such as dopamine and acetylcholine, which can alter neuronal excitability and synaptic transmission efficiency, thereby affecting visual information processing [46]. The current model may insufficiently account for mechanisms like dynamically changing synaptic plasticity and neuromodulation, restricting our analysis to the average performance of V1 within a specific timeframe post-stimulation and limiting exploration of fine regulatory phenomena across distinct temporal windows in V1.

The current model employs white square stimuli, which effectively focus on differences in surface-edge responses; however, stimuli in real visual scenes possess richer features. Studies have shown that the responses of V1 neurons to complex stimuli undergo significant changes due to complex factors such as texture density and color contrast [47–49], yet the present model has not incorporated encoding mechanisms for these features. For example, it remains worthy of consideration whether the "excitatory-inhibitory balance" in L2/3 still follows the current rules when stimuli contain gradient brightness or natural textures, and whether the intensity of surface inhibition is modulated by various more realistic and complex visual stimuli. In future work, we plan to introduce more details into the model, such as adding richer V1 cortical neuronal subtypes [10], further subdividing the categories of synaptic inputs received by neurons, and incorporating dynamically changing synaptic plasticity [44,45,50], thereby enriching our model to adapt to more complex and realistic visual stimuli.

Use of AI tools declaration

The authors declare they have not used Artificial Intelligence (AI) tools in the creation of this article.

Acknowledgments

This work was supported by the National Natural Science Foundation of China (Grant Nos. 12272092 and 12572067).

Conflict of interest

The authors declare there is no conflict of interest.

References

1. J. Rodrigues, J. M. du Buf, Multi-scale lines and edges in V1 and beyond: brightness, object categorization and recognition, and consciousness, *Biosystems*, **95** (2009), 206–226. https://doi.org/10.1016/j.biosystems.2008.10.006

2. S. Celebrini, S. Thorpe, Y. Trotter, M. Imbert, Dynamics of orientation coding in area V1 of the awake primate, *Visual Neurosci.*, **10** (1993), 811–825. https://doi.org/10.1017/s0952523800006052
3. H. S. Scholte, J. Jolij, H. Spekreijse, V.A.F. Lamme, Neural correlates of texture boundary detection and surface segregation are present in human V1, *J. Vision*, **3** (2003), 243. https://doi.org/10.1167/3.9.243
4. D. M. Alexander, C. V. Leeuwen, Mapping of contextual modulation in the population response of primary visual cortex, *Cognit. Neurodyn.*, **4** (2010), 1–24. https://doi.org/10.1007/s11571-009-9098-9
5. G. Zurawel, I. Ayzenshtat, S. Zweig, R. Shapley, H. Slovin, A contrast and surface code explains complex responses to black and white stimuli in V1, *J. Neurosci.*, **34** (2014), 14388–14402. https://doi.org/10.1523/JNEUROSCI.0848-14.2014
6. Y. Yang, T. Wang, Y. Li, W. Dai, G. Yang, C. Han, et al., Coding strategy for surface luminance switches in the primary visual cortex of the awake monkey, *Nat. Commun.*, **13** (2022), 286. https://doi.org/10.1038/s41467-021-27892-3
7. Z. Shay, G. Guy, R. Shapley, H. Slovin, Representation of color surfaces in V1: edge enhancement and unfilled holes, *J. Neurosci.*, **35** (2015), 12103–12115. https://doi.org/10.1523/JNEUROSCI.1334-15.2015
8. E. Baspinar, A. Sarti, G. Citti, A sub-Riemannian model of the visual cortex with frequency and phase, *J. Math. Neurosci.*, **10** (2020), 11. https://doi.org/10.1186/s13408-020-00089-6
9. G. Chen, F. Schuessler, W. Metzner, A data-based large-scale model for primary visual cortex enables brain-like robust and versatile visual processing, *Sci. Adv.*, **8** (2022). https://doi.org/10.1126/sciadv.abq7592
10. Y. N. Billeh, B. Cai, S. L. Gratiy, K. Dai, R. Iyer, N. W. Gouwens, et al., Systematic integration of structural and functional data into multi-scale models of mouse primary visual cortex, *Neuron*, **106** (2020), 388–403. https://doi.org/10.1016/j.neuron.2020.01.040
11. H. Yang, F. Han, Q. Wang, A large-scale neuronal network modelling study: stimulus size modulates gamma oscillations in the primary visual cortex by long-range connections, *Eur. J. Neurosci.*, **60** (2024), 4224–4243. https://doi.org/10.1111/ejn.16429
12. H. Yang, P. Wang, F. Han, Q. Wang, An interpretable mechanism for grating-induced cross-inhibition and gamma oscillation based on a visual cortical neuronal network model, *Electron. Res. Arch.*, **32** (2024), 2936–2954. https://doi.org/10.3934/era.2024134
13. J. Antolík, R. Cagnol, T. Rózsa, C. Monier, Y. Frégnac, A.P. Davison, et al., A comprehensive data-driven model of cat primary visual cortex, *PLoS Comput. Biol.*, **20** (2024), e1012342. https://doi.org/10.1371/journal.pcbi.1012342
14. Y. Jiang, G. Purushothaman, V. A. Casagrande, The functional asymmetry of ON and OFF channels in the perception of contrast, *J. Neurophysiol.*, **114** (2015), 2816–2829. https://doi.org/10.1152/jn.00560.2015
15. Y. J. Cao, C. Lin, Y. J. Pan, H. Zhao, Application of the center–surround mechanism to contour detection, *Multimed. Tools Appl.*, **78** (2019), 25121–25141. https://doi.org/10.1007/s11042-019-7722-1
16. E. A. Allen, R. D. Freeman, Dynamic spatial processing originates in early visual pathways, *J. Neurosci.*, **26** (2006), 11763–11774. https://doi.org/10.1523/JNEUROSCI.3297-06.2006

17. U. Bauer, M. Scholz, J. B. Levitt, K. Obermayer, J. S. Lund, A model for the depth-dependence of receptive field size and contrast sensitivity of cells in layer 4C of macaque striate cortex, *Vision Res.*, **39** (1999), 613–629. https://doi.org/10.1016/s0042-6989(98)00172-2
18. Y. Gonchar, A. Burkhalter, Distinct GABAergic targets of feedforward and feedback connections between lower and higher areas of rat visual cortex, *J. Neurosci.*, **23** (2003), 10904–10912. https://doi.org/10.1523/JNEUROSCI.23-34-10904.2003
19. X. Tie, S. Li, Y. Feng, B. Lai, S. Liu, B. Jiang, Distinct roles of NMDAR and mGluR5 in light exposure reversal of feedforward synaptic strength in V1 of juvenile mice after binocular vision deprivation, *Neuroscience*, **384** (2018), 131–138. https://doi.org/10.1016/j.neuroscience.2018.05.034
20. A. Alreja, I. Nemenman, C. J. Rozell, Constrained brain volume in an efficient coding model explains the fraction of excitatory and inhibitory neurons in sensory cortices, *PLoS Comput. Biol.*, **18** (2022), e1009642. https://doi.org/10.1371/journal.pcbi.1009642
21. H. Markram, M. Toledo-Rodriguez, Y. Wang, A. Gupta, G. Silberberg, C. Wu, Interneurons of the neocortical inhibitory system, *Nat. Rev. Neurosci.*, **5** (2004), 793–807. https://doi.org/10.1038/nrn1519
22. N. Fourcaud-Trocmé, D. Hansel, C. van Vreeswijk, N. Brunel, How spike generation mechanisms determine the neuronal response to fluctuating inputs, *J. Neurosci.*, **23** (2003), 11628–11640. https://doi.org/10.1523/JNEUROSCI.23-37-11628.2003
23. D. N. Scott, M. J. Frank, Adaptive control of synaptic plasticity integrates micro-and macroscopic network function, *Neuropsychopharmacology*, **48** (2023), 121–144. https://doi.org/10.1038/s41386-022-01374-6
24. C. Rivadulla, J. Sharma, M. Sur, Specific roles of NMDA and AMPA receptors in direction-selective and spatial phase-selective responses in visual cortex, *J. Neurosci.*, **21** (2001), 1710–1719. https://doi.org/10.1523/JNEUROSCI.21-05-01710.2001
25. L. Chariker, R. Shapley, L. S. Young, Orientation selectivity from very sparse LGN inputs in a comprehensive model of macaque V1 cortex, *J. Neurosci.*, **36** (2016), 12368–12384. https://doi.org/10.1523/JNEUROSCI.2603-16.2016
26. L. Chariker, R. Shapley, L. S. Young, Contrast response in a comprehensive network model of macaque V1, *J. Vis.*, **20** (2020), 16. https://doi.org/10.1167/jov.20.4.16
27. L. Campagnola, S. C. Seeman, T. Chartrand, L. Kim, A. Hoggarth, C. Gamlin, et al., Local connectivity and synaptic dynamics in mouse and human neocortex, *Science*, **375** (2022), eabj5861. https://doi.org/10.1126/science.abj5861
28. A. Stepanyants, J. A. Hirsch, L. M. Martinez, Z. F. Kisvárday, A. S. Ferecskó, D. B. Chklovskii, Local potential connectivity in cat primary visual cortex, *Cereb. Cortex*, **18** (2008), 13–28. https://doi.org/10.1093/cercor/bhm027
29. T. A. Hage, A. Bosma-Moody, C. A. Baker, M. B. Kratz, L. Campagnola, T. Jarsky, et al., Synaptic connectivity to L2/3 of primary visual cortex measured by two-photon optogenetic stimulation, *eLife*, **11** (2022), e71103. https://doi.org/10.7554/eLife.71103
30. T. W. Troyer, A. E. Krukowski, N. J. Priebe, K. D. Miller, Contrast-invariant orientation tuning in cat visual cortex: thalamocortical input tuning and correlation-based intracortical connectivity, *J. Neurosci.*, **18** (1998), 5908–5927. https://doi.org/10.1523/JNEUROSCI.18-15-05908.1998

31. J. Kremkow, L. U. Perrinet, C. Monier, J. M. Alonso, A. Aertsen, Y. Frégnac, et al., Push-pull receptive field organization and synaptic depression: mechanisms for reliably encoding naturalistic stimuli in V1, *Front. Neural Circuits*, **10** (2016), 37. https://doi.org/10.3389/fncir.2016.00037
32. M. M. Taylor, D. Contreras, A. Destexhe, Y. Frégnac, J. Antolik, An anatomically constrained model of V1 simple cells predicts the coexistence of push-pull and broad inhibition, *J. Neurosci.*, **41** (2021), 7797–7812. https://doi.org/10.1523/JNEUROSCI.0928-20.2021
33. P. Buzás, K. Kovács, A. S. Ferecskó, J. M. Budd, U. T. Eysel, Z. F. Kisvárday, Model-based analysis of excitatory lateral connections in the visual cortex, *J. Comp. Neurol.*, **499** (2006), 861–881. https://doi.org/10.1002/cne.21134
34. H. Ko, S. Hofer, B. Pichler, K. A. Buchanan, P. J. Sjöström, T. D. Mrsic-Flogel, Functional specificity of local synaptic connections in neocortical networks, *Nature*, **473** (2011), 87–91. https://doi.org/10.1038/nature09880
35. N. Voges, A. Schüz, A. Aertsen, S. Rotter, A modeler's view on the spatial structure of intrinsic horizontal connectivity in the neocortex, *Prog. Neurobiol.*, **92** (2010), 277–292. https://doi.org/10.1016/j.pneurobio.2010.05.001
36. T. Binzegger, R. J. Douglas, K. A. Martin, A quantitative map of the circuit of cat primary visual cortex, *J. Neurosci.*, **24** (2004), 8441–8453. https://doi.org/10.1523/JNEUROSCI.1400-04.2004
37. W. Li, V. Piëch, C. D. Gilbert, Contour saliency in primary visual cortex, *Neuron*, **50** (2006), 951–962. https://doi.org/10.1016/j.neuron.2006.04.035
38. H. You, G. Indiveri, D. R. Muir, Surround suppression explained by long-range recruitment of local competition, in a columnar V1 model, preprint, arXiv:1611.00945. https://doi.org/10.48550/arXiv.1611.00945
39. A. M. M. Oswald, B. Doiron, J. Rinzel, A. D. Reyes, Spatial profile and differential recruitment of GABAB modulate oscillatory activity in auditory cortex, *J. Neurosci.*, **29** (2009), 10321–10334. https://doi.org/10.1523/JNEUROSCI.1703-09.2009
40. O. W. Layton, E. Mingolla, A. Yazdanbakhsh, Neural dynamics of feedforward and feedback processing in figure-ground segregation, *Front. Psychol.*, **5** (2014), 972. https://doi.org/10.3389/fpsyg.2014.00972
41. O. W. Layton, E. Mingolla, A. Yazdanbakhsh, Dynamic coding of border-ownership in visual cortex, *J. Vis.*, **12** (2012), 8. https://doi.org/10.1167/12.13.8
42. O. W. Layton, A. Yazdanbakhsh, A neural model of border-ownership from kinetic occlusion, *Vision Res.*, **106** (2015), 64–80. https://doi.org/10.1016/j.visres.2014.11.002
43. E. Gao, Y. Yang, X. Sun, Dynamical regulation of hippocampal CA3 ripple oscillations by athorny pyramidal neurons, *Int. J. Dyn. Control*, **13** (2025), 358. https://doi.org/10.1007/s40435-025-01865-6
44. H. Markram, M. Tsodyks, Redistribution of synaptic efficacy between neocortical pyramidal neurons, *Nature*, **382** (1996), 807–810. https://doi.org/10.1038/382807a0
45. V. Chokshi, B. D. Grier, A. Dykman, C. L. Lantz, E. Niebur, E. M. Quinlan, et al., Naturalistic spike trains drive state-dependent homeostatic plasticity in superficial layers of visual cortex, *Front. Synaptic Neurosci.*, **13** (2021), 663282. https://doi.org/10.3389/fnsyn.2021.663282
46. M. Sarter, B. Givens, J. P. Bruno, The cognitive neuroscience of sustained attention: where top-down meets bottom-up, *Brain Res. Rev.*, **35** (2001), 146–160. https://doi.org/10.1016/s0165-0173(01)00044-3

47. J. Poort, M. W. Self, B. van Vugt, H. Malkki, P. R. Roelfsema, Texture segregation causes early figure enhancement and later ground suppression in areas V1 and V4 of visual cortex, *Cereb. Cortex*, **26** (2016), 3964–3976. https://doi.org/10.1093/cercor/bhw235
48. J. J. Knierim, D. C. van Essen, Neuronal responses to static texture patterns in area V1 of the alert macaque monkey, *J. Neurophysiol.*, **67** (1992), 961–980. https://doi.org/10.1152/jn.1992.67.4.961
49. T. Wachtler, T. J. Sejnowski, T. D. Albright, Representation of color stimuli in awake macaque primary visual cortex, *Neuron*, **37** (2003), 681–691. https://doi.org/10.1016/s0896-6273(03)00035-7
50. Y. S. Hwang, C. Maclachlan, J. Blanc, A. Dubois, C. C. H. Petersen, G. Knott, et al., 3D ultrastructure of synaptic inputs to distinct GABAergic neurons in the mouse primary visual cortex, *Cereb. Cortex*, **31** (2021), 2610–2624. https://doi.org/10.1093/cercor/bhaa378



AIMS Press

©2025 the Author(s), licensee AIMS Press. This is an open access article distributed under the terms of the Creative Commons Attribution License (https://creativecommons.org/licenses/by/4.0)